Extending the Polyol Reduction Process into the Second Dimension: Oxide Thin Film Reduction

Björn M. Stühmeier,[1,*] **Mark T. Greiner,**[2] **Vignesh Sureshwaran,**[1] **Lukas Schuster,**[1] **Li Hui Tiah,**[1] **Jan N. Schwämmlein,**[1,*,a] **Hubert A. Gasteiger,**[1,**] and **Hany A. El-Sayed**[1,z]

[1]*Chair of Technical Electrochemistry, Department of Chemistry, Technische Universität München, München, Germany*
[2]*Department of Heterogeneous Reactions, Max-Planck Institute for Chemical Energy Conversion, Mülheim an der Ruhr, Germany*

The formation of extended metal thin films (<5 nm) or monolayers on oxide surfaces, for applications in (electro-)catalysis, has never been achieved due to the high interfacial energy of the metal/oxide interface that always results in a 3D growth of the deposited metal. To realize 2D growth, the outermost surface of the oxide must be reduced prior to metal deposition in the same system. Here, we demonstrate that the polyol method, typically used for metal nanoparticles synthesis, can be used for the reduction of oxide thin films. The reduction of the oxide layer upon heating in ethylene glycol was electrochemically monitored in situ by measuring the open circuit potential and confirmed by cyclic voltammetry and near ambient pressure X-ray photoelectron spectroscopy. The reduction of oxide thin films could be verified for nanoparticles of Sn, Ni and Sb-doped SnO_2 in accordance with thermodynamic calculations. This method will enable the formation of metal thin films and monolayers on oxide substrates for applications in (electro-)catalysis.

Metal/oxide interfaces play important roles in several applications including microelectronics, materials science, and chemical applications, where the metal over-layer is in the form of particles, such as in catalysis, or thick films (>50 nm), such as in the semiconductor industry. The deposition of metallic monolayers or extremely thin films (<5 nm) on oxide surfaces, for applications in heterogeneous catalysis and electrocatalysis, has never been achieved due to the high interfacial energy of the metal/oxide interface that always results in a 3D morphology growth of the deposited metal.[1–4] To realize these structures, the metal/oxide interfacial tension has to be minimized, for example, by reducing the outermost surface of the oxide support before metal deposition.

In general, oxide reduction is achieved by either heating an oxide in the presence of a reducing agent, or by electrochemical means, such as aqueous or molten salt electrolysis.[5–10] In fine materials processing methods, electrochemical reduction has several advantages over gas phase reduction, including ease of use, precise control over the morphology, the possibility to accurately monitor the process via electrochemical means, and the ability to perform additional processing steps, such as metal deposition, in situ.[9–12] Such in situ techniques have been extensively used in synthesizing core–shell metallic nano-structures for application in the fields of (electro-)catalysis,[13–18] biology,[19] materials chemistry,[20,21] and sensors.[22,23]

Continuous metal films on high surface area supports are among the most promising structures for next generation electrode production in batteries and fuel cells.[24–29] To obtain these structures on oxide support materials, the outermost surface of the oxide must be reduced to form a metallic buffer layer on which metal deposition takes place. However, most surfaces re-oxidize after reduction treatment once the reducing agent is removed. Thus, successful pre-reduction should be performed directly before subsequent metallization steps, without removing the material from the reductant.

One wet chemical reduction method that has been extensively employed in the synthesis of (metal) nanoparticles,[30–34] could be very suitable for in situ surface processing steps. This method is based on polyols, such as ethylene glycol (EG), di-, tri, and tetraethylene glycol, or glycerol.[31] The polyols act as both solvent and reducing agent. They reduce solvated precursors to form metallic nanoparticles, and protect the nanoparticle surfaces from re-oxidation to enable subsequent metal deposition steps.[29,35–38] This technology would be very useful in electrode processing, if the reduction step can be additionally applied to solid surfaces, as it allows for uniform metallization of high surface area supports.

Here, we demonstrate that the polyol method can be used to reduce solid-state ions, specifically metal oxide surfaces, which is a completely new application of the polyol process. We show that metal oxide thin films, formed on bulk metallic substrates, metallic nanoparticles, and metal oxide nanoparticles, can be reduced by simply heating them in the appropriate polyalcohol, which would allow for a subsequent metal deposition step in the same solvent. In this system, the oxide reduction process can be in situ monitored, by measuring the electrode potential as a function of the temperature. The electrochemical means to monitor oxide reduction were confirmed by in situ near ambient pressure X-ray photoelectron spectroscopy (XPS) measurements. This polyol processing technique offers a low cost, easy to use, and highly adaptable method for a broad range of systems,[31–33] and will be a key processing technique in next generation fuel cell and battery electrode preparation.

Experimental

A modified polyol setup to monitor oxide reduction.—In order to investigate the reduction of an oxide thin film by monitoring the potential of the working electrode (a Sn oxide/Sn wire in this case) against a reference electrode (RE) as a function of solvent temperature, a typical polyol setup was modified as schematically shown in Fig. 1a. As the most suitable solvent for this study, EG was chosen as the most basic polyol and due to its dominant role in the synthesis of noble metal nanoparticles.[31] To avoid the high temperature of the system upon heating, a Ag/AgCl RE was not directly placed in the EG but separated by two electrolyte bridges (EBs) filled with the same polyol. Figure 1b shows the temperature
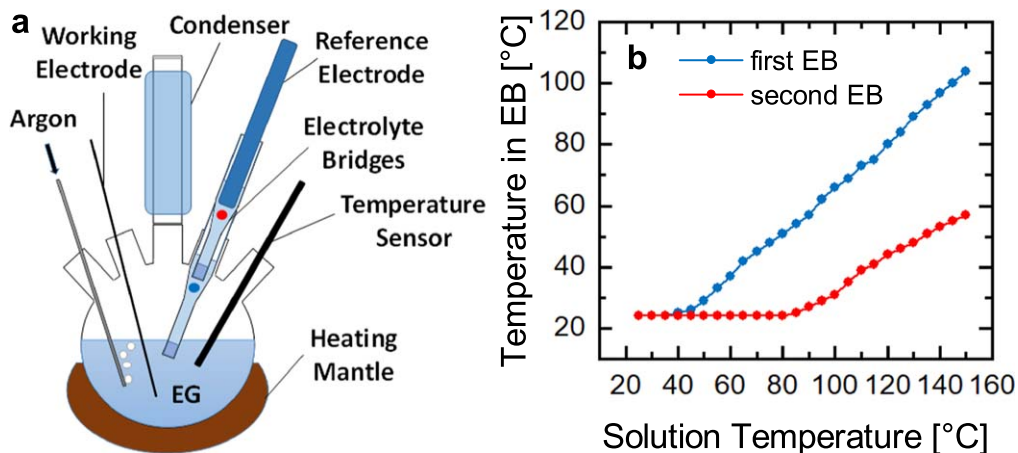
Figure 1. (a) Modified polyol setup used for monitoring the potential of the working electrode during the reduction by ethylene glycol; (b) temperature measured in the first and the second electrolyte bridge while heating the solution at 1 °C min^{-1}.
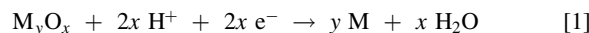
inside the first and second EBs, represented by the blue and red dots, respectively, as a function of EG temperature. Clearly, a single EB is not sufficient to prevent the RE from reaching the boiling temperature of the water-based RE electrolyte. However, when using two EBs, measurements until 180 °C can easily be achieved. Ar purging for 90 min with a flow rate of ca. 20 l h^{-1} was necessary to remove most soluble oxygen from the EG solvent. The potential of the working electrode was monitored at room temperature during the Ar purging. It was found that the potential gradually moves to more negative values with the Ar purging until a steady state potential was obtained indicating a constant concentration of oxygen in the solvent. This also suggests that the potential of the Sn electrode is mainly controlled by the O_2/H_2O redox equilibrium at room temperature. After 90 min of Ar purging the flow rate was reduced to 10 l h^{-1} during the experiment. The temperature of the system was increased with a ramp rate of 1 °C min^{-1} until the temperature reached the desired endpoint after which the system was allowed to cool down to room temperature at a rate of 1 °C min^{-1}. For measurements on nanoparticles, 10 μl of an ink consisting of 1.0 mg nanoparticles in 3.3 ml 2-propanol was drop casted onto the polished end of a glassy carbon rod (5 mm diameter), which served as the working electrode.

Cyclic voltammetry in the modified polyol setup.—All Cyclic voltammetry (CV) measurements were performed at room temperature in the modified polyol setup described above with a scan rate of 25 mV s^{-1}. For CV measurements at intermediate points during the heating cycle, the heating was interrupted at the indicated temperature and the reaction was flash-cooled to room temperature using an ice bath. To measure the potential more accurately, the EBs were removed and the RE was placed directly in the reaction vessel. A curled up gold wire was used as the counter electrode for the CV measurements. The measured currents were normalized to the exposed surface of the wire (calculated from the thickness and the electrolyte exposed length) or the area of the GC rod (0.196 cm^2), respectively.

X-ray photoelectron spectroscopy (XPS).—In-situ XPS measurements were performed using a Phoibos NAP-150 hemispherical analyzer from SPECS Surface Nanoanalysis GmbH. The excitation source was a monochromated Al k-α. A 1 cm × 1 cm piece of Sn foil was mounted onto a stainless steel sample holder. Prior to loading, the foil was cleaned by ultrasonication in acetone and deionized water. The sample was first measured in vacuum, as-loaded. The sample was then heated to 150 °C in an atmosphere of 0.1 mbar of EG. Heating was accomplished by illuminating the back-side of the sample holder with an infrared laser. Temperature was controlled using a calibration curve, whereby 3 W were required to heat the sample to 150 °C. The 0.1 mbar vapor pressure of EG was accomplished by dosing EG through an ultra-high vacuum leak

valve. EG was placed into a glass container, welded to a DN16-CF type flange, which was connected to the leak valve. The EG was degassed by several freeze-pump-thaw cycles, pumping to a turbomolecular pump, having a base pressure of 1 × 10^{-6} mbar. At room temperature, the ultimate pressure achievable when dosing EG was only 0.04 mbar. Therefore, we heated the EG up to 70 °C by wrapping the glass vessel in heating tape. At 70 °C a pressure of 0.1 mbar could be reached in the analysis chamber. A mass spectrometer (Pfeiffer Prisma), attached to the analysis chamber confirmed that EG, was being filled into the chamber. The mass spectrum showed a molecular peak of 62 AMU, as expected for EG.

Thermodynamic Calculations.—To examine the possibility of reducing bulk metal oxides, we first consider the thermodynamics of metal oxide reduction in a polyol medium (ethylene glycol). By considering the full reduction of the metal oxide MO_x to the corresponding metal (Eq. 1) and the full oxidation of EG to CO_2 (Eq. 2), and assuming standard conditions at the boiling point of the solvent, the Gibbs free energies (ΔG_{red}) for the reduction of numerous oxides were estimated previously.[39]

$$M_yO_x + 2x\,H^+ + 2x\,e^- \rightarrow y\,M + x\,H_2O \qquad [1]$$

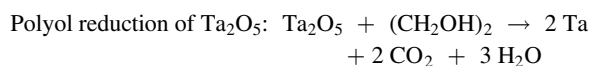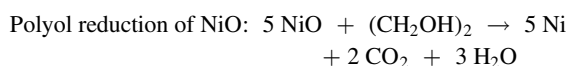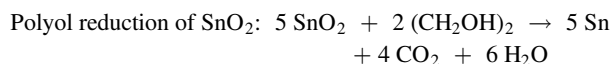$$(CH_2OH)_2 + 2\,H_2O \rightarrow 2\,CO_2 + 10\,H^+ + 10\,e^- \qquad [2]$$

While the oxidation of EG during the polyol process follows a much more complex reaction pathway,[40–42] such calculations provide a useful indication of what might thermodynamically be possible. Thus, the Gibbs free energies of the reduction of three metal oxides (tin, nickel, and tantalum oxides) using EG were calculated as a function of temperature ($\Delta_{red}G(T)$) under otherwise standard conditions (pressures/activities) using the standard enthalpy of formation ($\Delta_f H_i^{\varnothing}$) for the reactants and the standard entropy ($S_i^{\varnothing}$) for each compound at 25 °C, assuming that the entropy term is not a function of temperature within the investigated temperature range (Eq. 3).[43] For the calculation of the Gibbs free energy of reduction under more realistic conditions, the initial activities (a_i) of reactants and products were taken into account (Eq. 4) using Raoult's law (Eq. 5).[43] In our experimental setup, an initial concentration of 100 ppm of H_2O was measured by Karl Fischer titration and the maximum partial pressure (p_i) of CO_2 was estimated to be 40 ppm, i.e., 10% of the partial pressure of CO_2 in air (under the condition of continuous purging with Ar). The activities of EG and all solid reactants were assumed to equal 1.

$$\Delta_{red}G(T) = \sum_i \nu_i \Delta_f H_i^{\varnothing} - T\sum_i \nu_i S_i^{\varnothing} \qquad [3]$$

$$\Delta_{red}G(T, a_i) = \sum_i \nu_i \Delta_f H_i^{\varnothing} - T \sum_i \nu_i S_i^{\varnothing} + RT \ln\left(\prod_i a_i^{\nu_i}\right) \quad [4]$$

$$a_i = \frac{p_i}{p_i^{\varnothing}} \approx \chi_i \quad [5]$$

Exemplarily, the Gibbs free energy was calculated for the reduction of tin, nickel and tantalum oxide assuming the following reaction equations (thermodynamic values given in Table S1 available online at stacks.iop.org/JES/168/014506/mmedia):

Polyol reduction of SnO_2: $5\,SnO_2 + 2\,(CH_2OH)_2 \rightarrow 5\,Sn + 4\,CO_2 + 6\,H_2O$

Polyol reduction of NiO: $5\,NiO + (CH_2OH)_2 \rightarrow 5\,Ni + 2\,CO_2 + 3\,H_2O$

Polyol reduction of Ta_2O_5: $Ta_2O_5 + (CH_2OH)_2 \rightarrow 2\,Ta + 2\,CO_2 + 3\,H_2O$

When comparing the Gibbs fee energies of reduction under standard conditions (Fig. 2a) to more realistic conditions, taking the initial activities of reactants and products into account (Fig. 2b), it can be seen that, while nickel oxide may be reduced by EG even at room temperature and standard conditions, tantalum oxide cannot be reduced even up to the boiling temperature of EG. The calculations for tin oxide showed that, at standard conditions, it cannot be reduced by EG up to 200 °C. However, when reduced activities for CO_2 and H_2O were considered, the results suggested that tin oxide could be reduced by EG even at room temperature.

Results

The measurement of such reduction processes is not trivial for oxide nanoparticles dispersed and heated in EG. To facilitate the monitoring of oxide reduction, initial experiments were carried out to reduce oxide thin films on their corresponding metal substrates. This was achieved by dipping a Sn wire covered with native Sn oxide (Sn oxide/Sn) of an approximate thickness of 2-4 nm (a surface oxide thickness expected after long time exposure to air)[44,45] in EG and monitoring the potential vs a reference electrode. Lithium bis(trifluoromethanesulfonyl)imide (LiTFSI) was added to the EG to ensure sufficient ionic conductivity for in situ electrochemical characterization, while oxygen was removed by purging with argon to prevent re-oxidation.

The potential in any system is the result of a charge separation across the interface of two conducting phases.[46] Thus, a sudden change in potential would be expected upon reduction of the oxide layer, due to the different surface-electrolyte interaction between a semiconducting oxide and a metal electrode.[47] Figure 3a shows the change in the Sn oxide/Sn electrode potential, vs Ag/AgCl, as a function of EG temperature (1 °C min^{-1} ramp rate).

It can be clearly seen that there are three distinguishable stages during the heating ramp. At stage I, a linear behavior of the potential vs temperature was observed, followed by a sudden decrease in the measured potential (stage II), and then a steady-state potential was obtained (stage III). The potential drop may indicate oxide thin film reduction, and a steady-state potential most likely indicates that no further changes (namely oxide reduction) are taking place,[46] although the temperature is still increasing, which suggests that the oxide reduction process has been completed.

Based on a typical polyol method, in which solvated metal ions are reduced to form metal nanoparticles, the behavior observed here is what is expected for the reduction of an oxide. For a metal ion to be reduced by a polyol, as long as it is thermodynamically favorable, a reaction barrier between the reduction potential of metal ions and the oxidation potential of polyol must be overcome by heating the polyol.[44] Therefore, in metal ion reduction, no substantial physical changes are observed until a significant reduction takes place at a threshold temperature, after which the color of the solution changes dramatically, indicating the formation of nanoparticles. Thermodynamically, oxide reduction can start at temperatures as low as 30 °C (Fig. 2b), but the reaction might still be kinetically hindered. This can be attributed to the time needed to reduce the oxide film and reveal the metal underneath it. According to our hypothesis, the potential drop starts only when the underlying metal is exposed to the EG, which requires reduction of the oxide film on top. In other words, it is possible that oxide reduction starts at low temperature, but the potential drop takes place only after consuming enough oxide to reveal the underlying metal.

In fact, clear signs of reduction, i.e. a change in the slope of the OCP-temperature profile resulting in a sudden potential drop, start at a threshold temperature of around 60 °C and continue until the oxide film has been fully reduced, after which a steady-state potential is reached. Upon cooling, this steady-state potential is maintained, indicating that the surface does not re-oxidize in the Ar-saturated electrolyte, confirming that the reduction is indeed kinetically hindered rather than the reduced surface being thermodynamically instable.

When performing a second heating cycle, following the reduction, the potential decrease is marginal compared to the distinct drop during the first heating ramp. This shows that the reduction had been
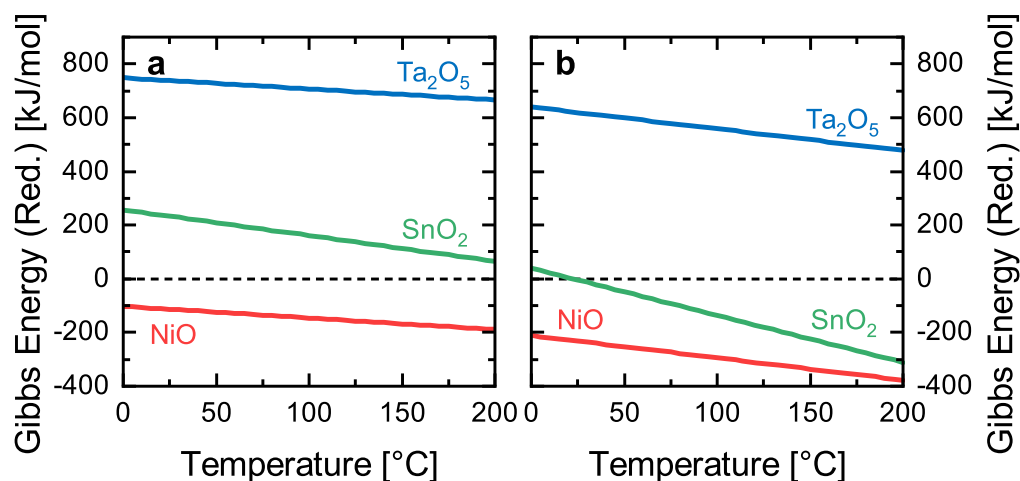

Figure 2. Gibbs free energy calculated for oxide reduction with EG to the corresponding metal at (a) standard conditions and (b) non-standard conditions (40 ppm CO_2 and 100 ppm H_2O).
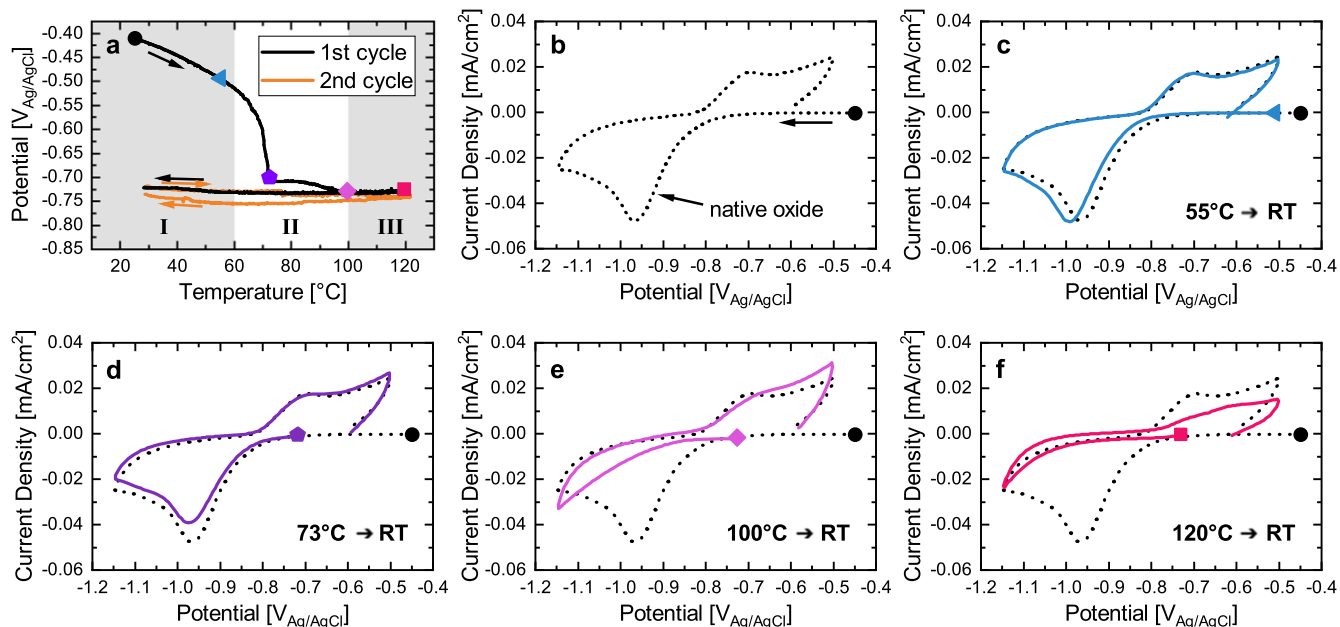
Figure 3. Chemical reduction of the native oxide thin layer on a Sn wire in ethylene glycol containing 0.25 M LiTFSI; (a) OCP-temperature profile with three distinguishable stages (I—III) and intermediate points used for electrochemical characterization; (b) CV of a fresh Sn wire; (c)–(f) CVs recorded at intermediate points during the reduction (after flash-cooling from the indicated temperature to room temperature) compared to the fresh wire showing increasing reduction of the native oxide. All CVs were recorded at room temperature (RT, 15–25 °C) at 25 mV s^{-1}.

completed during the first cycle, and little to no re-oxidation by residual oxygen had occurred. To check this hypothesis, cyclic voltammetry (CV) measurements were performed at various stages of the reduction process (Figs. 3b–3f) using a fresh wire for each experiment and normalizing the current to the surface area exposed

to the electrolyte. CVs were conducted in the polyol solution in the presence of a conducting salt at room temperature after flash-cooling the solution from different temperature points of the heating cycle. When starting at the open circuit potential (OCP) of a fresh Sn wire, a reductive peak at -0.96 V (vs Ag/AgCl; $V_{Ag/AgCl}$) is observed
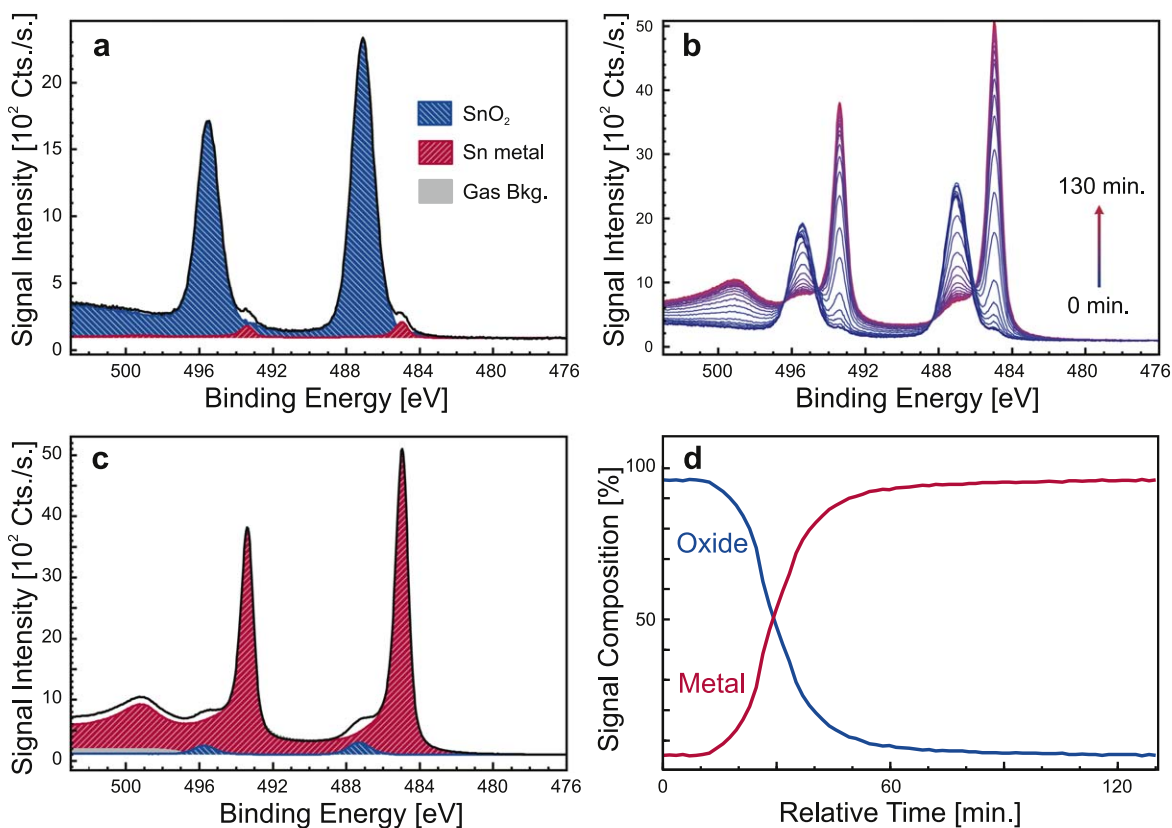

Figure 4. Near ambient pressure XPS showing the reduction of the native tin oxide thin film by EG. (a) Sn 3d signal of a fresh sample showing mainly tin oxide; (b) development of the Sn 3d signal upon heating to 150 °C in 0.1 mbar EG atmosphere; (c) Sn 3d signal after reduction; (d) partial contributions of the tin oxide and the elemental tin signal as a function of heating time.

during the negative going scan, corresponding to the reduction of the native oxide thin film (Fig. 3b). At the end of stage I (Fig. 3c), the reductive feature had shifted to slightly more negative potentials, most likely due to flash-cooling the solution below room temperature resulting in slower reduction kinetics,[48] but the total charge remained the same, indicating that no reduction has occurred. After the initial potential drop at ≈70 °C (Fig. 3d), the reductive feature had decreased slightly compared to that of a fresh Sn wire, indicating the onset of the reduction. This implies that the potential drop is due to the oxide reduction, revealing metallic Sn, and that the intermediate potential plateau during stage II could be the result of a mixed potential region with Sn oxide and Sn surface being exposed while the reduction continues. After the second potential drop of stage II at ≈100 °C, the reductive feature had mostly disappeared (Fig. 3e), and when the wire had been heated to the final temperature of 120 °C, no further reduction could be observed during the CV (Fig. 3f), proving that the oxide reduction process has been completed on all surfaces that were in contact with EG and in turn electrochemically accessible by the electrolyte. A similar drop in the OCP has been observed when heating a Sn wire in pure EG indicating that the method of measuring the OCP can be applied to systems without additional conducting salts as well (Fig. S1). However, due to the low ionic conductivity in pure EG, the reduction could not be verified by measuring CVs.

To confirm that the reduction of SnO_2 occurs in pure EG, near ambient pressure XPS was performed on a Sn foil to monitor the reduction in situ. The initial spectra of the sample, upon loading into vacuum from air, showed that the sample exhibited no signs of contamination except for the "adventitious carbon" signal typical for samples having been exposed to air.[49] The Sn 3d signal revealed signs of a thin native oxide layer formed on the foil, as evident from the oxidized Sn signal at a binding energy of ca. 487.1 eV.[50] One can also discern a weak signal from metallic Sn, at a binding energy of ca. 485.0 eV (Fig. 4a).[51] These observations suggest that the metallic Sn is buried under an oxide of ca. 6 nm thickness (based on the Sn^0 relative to the Sn^{4+} signal intensity, and assuming an inelastic mean free path of 2 nm, for electrons with 1000 eV kinetic energy in SnO_2). Note that an accurate determination of the Sn:O stoichiometry in the oxide film was not possible, due to the presence of the adventitious carbon (which also contains oxygen), and due to the fact that the oxide film was so thin, its signal has not converged to its bulk value. Nonetheless, a rough approximation of the Sn:O ratio, whereby these factors are ignored, gives a Sn-to-O ratio of 3:7, which is close to the 3:6 ratio one would expect for SnO_2. Thus we conclude that the native oxide was likely composed of SnO_2.

After heating the Sn foil in EG (0.1 mbar) to 150 °C, the Sn 3d signal of the metallic component slowly starts to rise, while the signal of the oxidized component slowly decreases (Fig. 4b). The transition continues, and slows down to a near steady state after ca. 120 min (Fig. 4c). After this time, some small amount of oxidized Sn could still be discerned in the spectrum, equating to roughly 5% of the initial SnO_2 signal intensity (Fig. 4d). Presumably, a higher pressure of EG or a higher temperature would eventually completely reduce this species. These results with EG vapor further prove that the reduction of the oxide film is achieved without dissolving the metal ions as it would be the case in a classical polyol process.[34]

Discussion

Having shown that EG is capable of reducing the native oxide layer on bulk Sn by two in situ techniques, the potential of Sn nanoparticles (NPs, <150 nm), drop-casted onto a glassy carbon (GC) disc, was measured in the LiTFSI-modified polyol setup to check whether this method can be applied to nanoparticles as well. Sn nanoparticles are also covered with a thin layer of Sn oxide, where the composition/thickness of this oxide depends on the synthesis method.[52] The OCP-temperature profile shows a potential drop that starts around 95 °C, followed by a second potential drop beginning at 150 °C (Fig. 5a). This indicates that the Sn oxide thin

film on nanoparticles might be more resistive to reduction than that on a flat Sn substrate, as would be expected due to the particle size effect on the surface energy that shifts the redox equilibrium towards the oxide for smaller particles.[53] Additionally, the contact between the nanoparticles forming the film may result in a reduced accessibility by EG, thus requiring more time and higher temperatures for the reduction. The absence of a hysteresis between the first and the second heating ramps in addition to a potential difference of about 470 mV between initial and final state indicate that oxide reduction has successfully taken place. Again, the reduction could be confirmed by the disappearance of the native oxide reduction feature in the CV after the heating cycle (Fig. 5b).

The thermodynamic calculations (Fig. 2) suggested that the reduction of NiO by EG should be possible, while Ta_2O_5 should be unreducible even at 200 °C. Having established that a distinct drop in potential shows the reduction of the native oxide thin film, further experiments were carried out to prove the general applicability of the method. As expected, the initial potential drop, indicating the start of oxide reduction, occurred at a relatively low temperature of ≈40 °C when using a Ni wire (Fig. 6a). Interestingly, the potential during the second heating cycle perfectly overlapped with the cooling branch of the first cycle, indicating that the reductive strength of EG was sufficient to prevent any re-oxidation of nickel by traces of oxygen in the system. Again, for nickel nanoparticles (<100 nm), the reduction took place at higher temperatures compared to a flat substrate, with no further reduction observable during a second heating cycle (Fig. 6c). On the contrary, the potential returned to the initial state when a tantalum wire was heated in EG, indicating that no reduction of tantalum oxide had taken place (Fig. 6b). Still, a hysteresis in the potential-temperature profile was observed which may hint towards a reversible interaction between EG and tantalum oxide that is kinetically hindered.

To this point, surface oxide reduction has merely been shown on native oxide thin films on metal substrates. However, the general applicability of using the polyol process for the reduction of surface oxides would require that it is possible to reduce the surface of bulk oxides as well. Thus, nanoparticles of antimony-doped tin oxide (ATO, <50 nm), which are sufficiently conductive to allow for monitoring the potential, were investigated (Fig. 6d). According to the previous observations, the two distinct potential drops, starting at ≈60 °C and ≈140 °C, respectively, and a potential difference of ≈170 mV at room temperature after the heating cycle strongly indicate that the reduction of the ATO surface was successful.

To demonstrate the general applicability of the newly discovered phenomenon, Fig. 7 shows the Gibbs free energy of reduction of a large number of oxides, using EG, plotted against temperature (both at standard and non-standard conditions). Figure 7a shows that there is a broad spectrum of oxides that can be readily reduced by EG, even at room temperature, for instance, NiO, CuO, Co_3O_4, IrO_2 and MoO_3. Some oxides, like Fe_2O_3, can be reduced by EG at elevated temperatures, and numerous oxides cannot be reduced even at EG's boiling temperature, e.g., SnO_2, WO_3, Al_3O_4 and ZnO. We have shown earlier that Sn oxide can be reduced by EG if the non-standard conditions are considered in the calculation.

Figure 7b, in which the non-standard conditions were considered in the calculation, shows that other than SnO_2, there are a few metal oxides that can be reduced by EG when the water content and CO_2 concentrations are low enough. These oxides include In_2O_3, Fe_3O_4, and WO_3. The comparison between Fig. 7a and b shows that the lines representing these metal oxides have moved below the zero line and thus they thermodynamically can be reduced by EG (if a full oxidation to CO_2 is assumed). In Fig. 7c, the reduction of SnO_2 to Sn is calculated for a variety of (poly)alcohols assuming full oxidation to CO_2 and H_2O, and non-standard conditions (the calculations needed to obtain this figure are provided in the SI). While these thermodynamic calculations obviously neglect the complexity of the reduction reaction, they indicate that by tuning the reaction conditions, e.g. reducing the concentration of the side products H_2O and CO_2, and choosing a suitable (poly)alcohol, it is possible to reduce
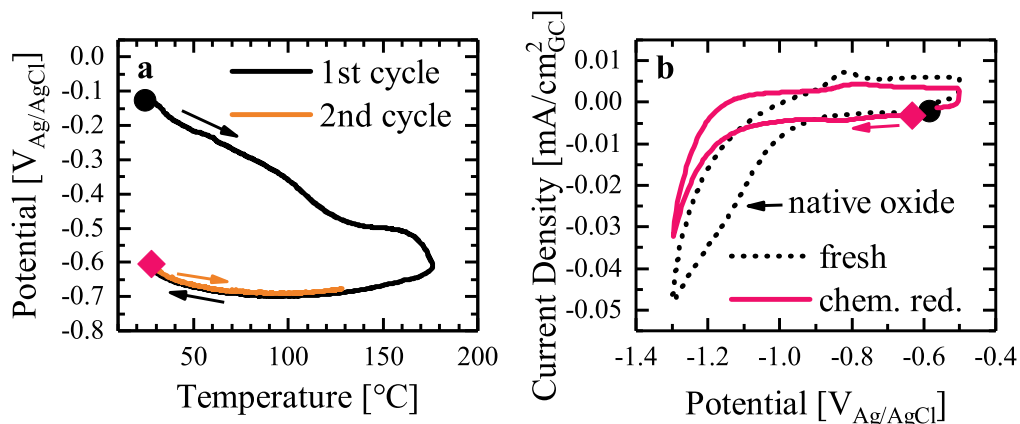
Figure 5. Chemical reduction of the native oxide thin layer on Sn nanoparticles in ethylene glycol containing 0.25 M LiTFSI; (a) OCP-temperature profile of the chemical reduction and electrochemical characterization points; (b) comparison of the CVs of fresh vs chemically reduced Sn nanoparticles (scan rate: 25 mV s^{-1}).
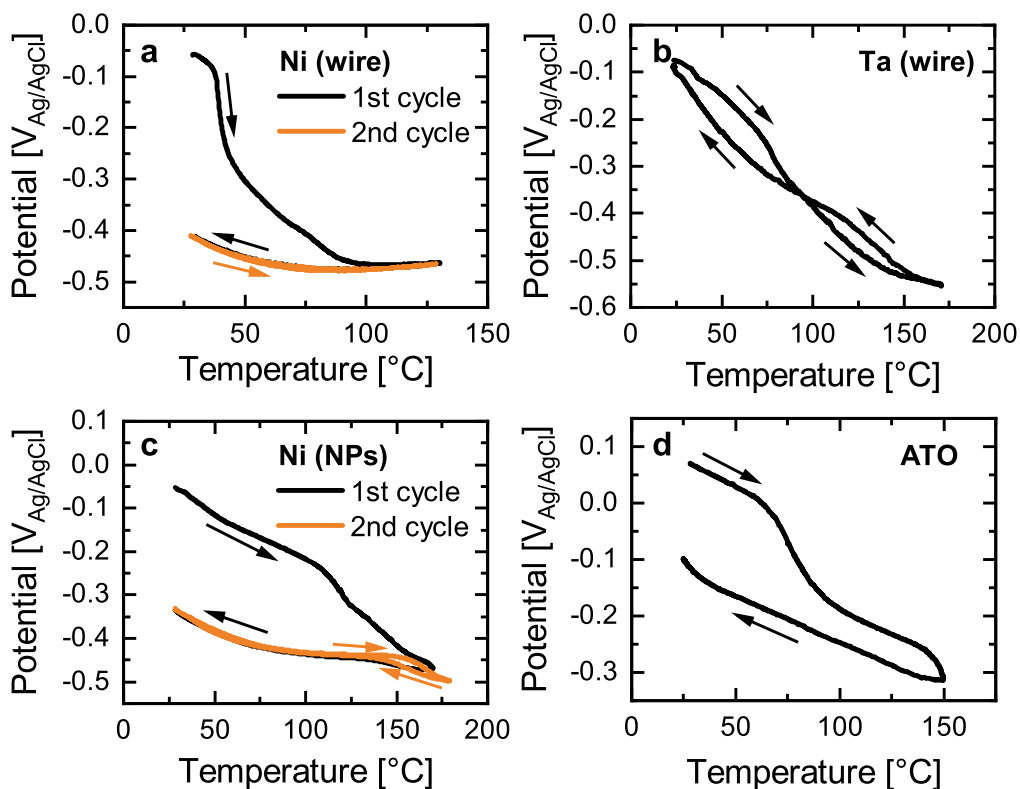

Figure 6. OCP-temperature profiles of (a) a Ni wire; (b) a Ta wire; (c) Ni nanoparticles; and (d) Sb-doped Sn oxide (ATO) nanoparticles while heated in ethylene glycol containing 0.25 M LiTFSI.

the surface of a broad range of metal oxides. It could be confirmed by near ambient pressure XPS that indeed methanol is capable of reducing the native SnO_2 layer on a Sn substrate (data not shown).

Conclusions

The results presented in this study clearly demonstrate that the polyol method is an efficient process in reducing oxide thin films on extended surfaces as well as on nanostructures. It was further shown that the reduction of these oxides can be in situ monitored by cyclic voltammetry when adding a conductive salt, e.g. LiTFSI. A drop in OCP was established as a clear indication for the reduction of an oxide thin film, thus allowing for a simple method to monitor the reduction process. In-situ recorded near ambient pressure XPS directly showed the reduction of the native oxide layer on a Sn

substrate by EG at elevated temperatures, thus verifying the electrochemical measurements. By OCP measurements, we have shown that EG can reduce both Sn and Ni oxides, but it is not capable of reducing Ta oxide under relevant conditions, and up to the boiling temperature of the solvent. The new oxide reduction process is independent of the oxide morphology (extended surfaces, nanoparticles and nanowires), so it can have a technological impact on metal coatings on oxide surfaces where the coating can be now done through a metallic buffer layer as shown here. Oxide$_{core}$-metal$_{shell}$ structures may now be obtained on any oxide particle shape,[54] which was limited in the past to surface modified metal oxides[54] or the use of metallic nanoparticles as intermediates for the shell formation.[55,56] Using this new approach, the surface of oxide particles of various shapes can be reduced, and so a metal
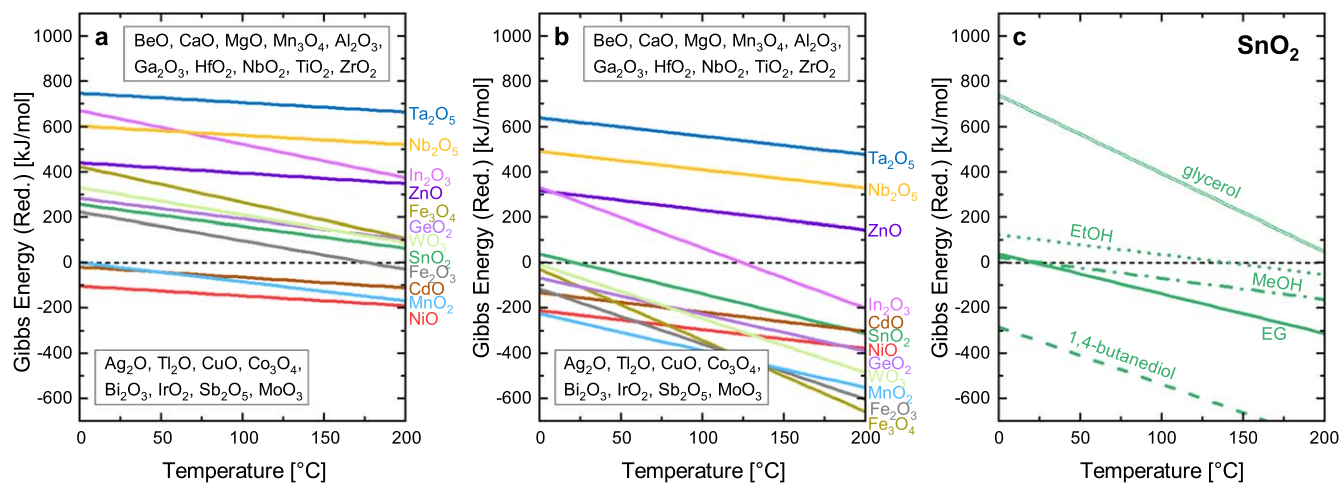
Figure 7. Gibbs free energy calculated for the reduction with EG to the corresponding metal at (a) standard conditions and (b) non-standard conditions (40 ppm CO_2 and 100 ppm H_2O). Metal oxides given in the boxes have a clearly positive (top right) or negative (bottom left) Gibbs free energy of reduction; (c) Gibbs free energy for the reduction of SnO_2 by various (poly)alcohols at non-standard conditions.

layer may be coated on top of it via the polyol method, which is a process we are currently investigating.

ORCID

Björn M. Stühmeier https://orcid.org/0000-0001-7713-2261
Jan N. Schwämmlein https://orcid.org/0000-0001-8902-4508
Hubert A. Gasteiger https://orcid.org/0000-0001-8199-8703

References

1. Q. Fu and T. Wagner, *Surf. Sci. Rep.*, **62**, 431 (2007).
2. J. Lu, K.-B. Low, Y. Lei, J. A. Libera, A. Nicholls, P. C. Stair, and J. W. Elam, *Nat. Commun.*, **5**, 3264 (2014).
3. N. W. Kwak, S. J. Jeong, H. G. Seo, S. Lee, Y. Kim, J. K. Kim, P. Byeon, S.-Y. Chung, and W. Jung, *Nat. Commun.*, **9**, 4829 (2018).
4. K. Sarakinos, *Thin Solid Films*, **688**, 137312 (2019).
5. A. F. Hollemann, E. Wiberg, and N. Wiberg, *Lehrbuch der anorganischen Chemie, 102. Auflage* (Walter de Gruyter, Berlin, New York) (2007).
6. S. Luidold and H. Antrekowitsch, *JOM*, **59**, 20 (2007).
7. C. R. O'Connor, M. A. van Spronsen, T. Egle, F. Xu, H. R. Kersell, J. Oliver-Meseguer, M. Karatok, M. Salmeron, R. J. Madix, and C. M. Friend, *Nat. Commun.*, **11**, 1844 (2020).
8. A. Borgschulte, O. Sambalova, R. Delmelle, S. Jenatsch, R. Hany, and F. Nüesch, *Sci. Rep.*, **7**, 40761 (2017).
9. W. Xiao and D. Wang, *Chem. Soc. Rev.*, **43**, 3215 (2014).
10. J. N. Schwämmlein, P. A. L. Torres, H. A. Gasteiger, and H. A. El-Sayed, *Sci. Rep.*, **10**, 59 (2020).
11. G. Z. Chen, D. J. Fray, and T. W. Farthing, *Nature*, **407**, 361 (2000).
12. A. M. Abdelkader, K. T. Kilby, A. Cox, and D. J. Fray, *Chem. Rev.*, **113**, 2863 (2013).
13. J. Kibsgaard, Z. Chen, B. N. Reinecke, and T. F. Jaramillo, *Nat. Mater.*, **11**, 963 (2012).
14. M. B. Gawande, A. Goswami, T. Asefa, H. Guo, A. V. Biradar, D.-L. Peng, R. Zboril, and R. S. Varma, *Chem. Soc. Rev.*, **44**, 7540 (2015).
15. L. Tzounis, C. Gravalidis, A. Papamichail, and S. Logothetidis, *Materials Today: Proceedings*, **3**, 832 (2016).
16. R. Jiang, S. o. Tung, Z. Tang, L. Li, L. Ding, X. Xi, Y. Liu, L. Zhang, and J. Zhang, *Energy Storage Mater.*, **12**, 260 (2018).
17. M. Luo, Y. Yang, Y. Sun, Y. Qin, C. Li, Y. Li, M. Li, S. Zhang, D. Su, and S. Guo, *Mater. Today*, **23**, 45 (2019).
18. W. Lamai, A. Bunphung, I. Junumpun, and A. Wongkaew, *Materials Today: Proceedings*, **17**, 1396 (2019).
19. A.-M. Hada, M. Potara, S. Suarasan, A. Vulpoi, T. Nagy-Simon, E. Licarete, and S. Astilean, *Nanotechnology*, **30**, 315701 (2019).
20. A. Pajor-Świerzy, D. Gaweł, E. Drzymała, R. Socha, M. Parlińska-Wojtan, K. Szczepanowicz, and P. Warszyński, *Nanotechnology*, **30**, 015601 (2018).
21. P. Bhatia, S. S. Verma, and M. M. Sinha, *Chem. Phys. Lett.*, **745**, 137272 (2020).
22. A. Härtl, E. Schmich, J. A. Garrido, J. Hernando, S. C. R. Catharino, S. Walter, P. Feulner, A. Kromka, D. Steinmüller, and M. Stutzmann, *Nat. Mater.*, **3**, 736 (2004).
23. P. K. Kalambate, Dhanjai, Z. Huang, Y. Li, Y. Shen, M. Xie, Y. Huang, and A. K. Srivastava, *TrAC, Trends Anal. Chem.*, **115**, 147 (2019).
24. S. H. Joo, J. Y. Park, C.-K. Tsung, Y. Yamada, P. Yang, and G. A. Somorjai, *Nat. Mater.*, **8**, 126 (2009).
25. D. F. van der Vliet, C. Wang, D. Tripkovic, D. Strmcnik, X. F. Zhang, M. K. Debe, R. T. Atanasoski, N. M. Markovic, and V. R. Stamenkovic, *Nat. Mater.*, **11**, 1051 (2012).
26. K. Y. Cho, Y. S. Yeom, H. Y. Seo, P. Kumar, K.-Y. Baek, and H. G. Yoon, *J. Mater. Chem. A*, **5**, 3129 (2017).
27. H. Wang, H. Yu, S. Yin, Y. Xu, X. Li, Y. Yamauchi, H. Xue, and L. Wang, *J. Mater. Chem. A*, **6**, 12744 (2018).
28. Z. Wang, Q. Gao, P. Lv, X. Li, X. Wang, and B. Qu, *J. Mater. Sci. Technol.*, **38**, 119 (2020).
29. Y.-C. Hsieh et al., *Nat. Commun.*, **4**, 2466 (2013).
30. S. Alayoglu, A. U. Nilekar, M. Mavrikakis, and B. Eichhorn, *Nat. Mater.*, **7**, 333 (2008).
31. F. Fiévet, S. Ammar-Merah, R. Brayner, F. Chau, M. Giraud, F. Mammeri, J. Peron, J. Y. Piquemal, L. Sicard, and G. Viau, *Chem. Soc. Rev.*, **47**, 5187 (2018).
32. S. Nam, B. Park, and B. D. Condon, *RSC Adv.*, **8**, 21937 (2018).
33. I. Favier, D. Pla, and M. Gómez, *Chem. Rev.*, **120**, 1146 (2020).
34. H. Dong, Y. C. Chen, and C. Feldmann, *Green Chem.*, **17**, 4107 (2015).
35. G. Park, D. Seo, J. Jung, S. Ryu, and H. Song, *J. Phys. Chem. C*, **115**, 9417 (2011).
36. N. V. Long, T. Asaka, T. Matsubara, and M. Nogami, *Acta Mater.*, **59**, 2901 (2011).
37. H. Zhu, X. Li, and F. Wang, *Int. J. Hydrogen Energy*, **36**, 9151 (2011).
38. J. N. Schwämmlein, B. M. Stühmeier, K. Wagenbauer, H. Dietz, V. Tileli, H. A. Gasteiger, and H. A. El-Sayed, *J. Electrochem. Soc.*, **165**, H229 (2018).
39. D. Larcher and R. Patrice, *J. Solid State Chem.*, **154**, 405 (2000).
40. M. J. González, C. T. Hable, and M. S. Wrighton, *J. Phys. Chem. B*, **102**, 9881 (1998).
41. T. Matsumoto, K. Takahashi, K. Kitagishi, K. Shinoda, J. L. Cuya Huaman, J.-Y. Piquemal, and B. Jeyadevan, *New J. Chem.*, **39**, 5008 (2015).
42. H. A. El-Sayed, V. M. Burger, M. Miller, K. Wagenbauer, M. Wagenhofer, and H. A. Gasteiger, *Langmuir*, **33**, 13615 (2017).
43. P. Atkins and J. De Paula, , *Atkins' Physical Chemistry* 10th edn. ed.(Oxford Univ. Press, Oxford) (2014).
44. S. Cho, J. Yu, S. K. Kang, and D.-Y. Shih, *J. Electron. Mater.*, **34**, 635 (2005).
45. P. Song and D. Wen, *J. Phys. Chem. C*, **113**, 13470 (2009).
46. A. J. Bard and L. R. Faulkner, *Electrochemical Methods: Fundamentals and Applications* (Wiley, Hoboken) (2001).
47. N. Sato, *Electrochemistry at Metal and Semiconductor Electrodes* (Elsevier, Amsterdam) (1998).
48. S. Hadži-Jordanov, *J. Electrochem. Soc.*, **125**, 1471 (1978).
49. T. L. Barr and S. Seal, *J. Vac. Sci. Technol. A*, **13**, 1239 (1995).
50. M. A. Stranick and A. Moskwa, *Surf. Sci. Spectra*, **2**, 50 (1993).
51. J. F. Moulder, W. F. Stickle, and P. E. Sobol, *Handbook of X-ray Photoelectron Spectroscopy* (Perkin-Elmer, Physical Electronics Division, Eden Prairie) (1993).
52. S. Nakayama, T. Sugihara, J. Matsumoto, T. Notoya, and T. Osakai, *J. Electrochem. Soc.*, **158**, C341 (2011).
53. A. Navrotsky, C. Ma, K. Lilova, and N. Birkner, *Science*, **330**, 199 (2010).
54. E. A. Kwizera, E. Chaffin, Y. Wang, and X. Huang, *RSC Adv.*, **7**, 17137 (2017).
55. J. C. M. Silva, R. F. B. De Souza, L. S. Parreira, E. T. Neto, M. L. Calegaro, and M. C. Santos, *Appl. Catal., B*, **99**, 265 (2010).
56. V. M. Dhavale and S. Kurungot, *J. Phys. Chem. C*, **116**, 7318 (2012).